CHAPTER 2

Experimental

GLENDOWER: I can call spirits from the vasty deep.

HOTSPUR: Why, so can I, or so can any man;

But will they come when you do call for them?

-William Shakespeare

The First Part of King Henry the Fourth

Infrared methods

The investigations described in this thesis all involve the detection of infrared light. Most of the studies are based on direct absorption of high resolution, tunable cw infrared laser light. Fourier Transform Infrared (FTIR) emission studies are also an important part of this work. In some of the studies IR detection is intrinsically mandated, as in our measurements of the rovibrational radiative lifetimes of OH. In other cases the IR methods are not necessary *per se*, but are convenient and sensitive probes with high resolution of vibrational and rotational states, as well as velocities. Before describing the details of the experimental arrangements, it should be noted that one of the most powerful aspects of the infrared laser absorption method isits generality. Most species absorb in the infrared. Thus, while the experimental techniques are described with specific molecules in mind, the techniques are readily extended to a large variety of systems. Also, the techniques of high resolution IR absorption and emission

are, of course, well established and by no means unique to our group; numerous examples from many branches of chemical physics appear throughout this thesis.

The OH experiments are carried out with a high resolution infrared flash kinetic spectrometer. This spectrometer is based on a 1 m flow cell through which HNO_3 or H_2O_2 and any desired reactant gas is flowed in a large excess of buffer gas. The OH radicals are produced by a 10 ns 193 nm or 248 nm laser pulse which traverses the length of the cell, and are probed along the same path via time-resolved, weak fractional absorption of IR light from a color center laser tuned to a set of rotational, spin orbit, and λ doublet resolved transitions in the $v=1\leftarrow0$ vibrational manifold. The specific advantages of this arrangement are detailed in each chapter of this thesis. However, several general properties are worth mentioning at the outset. i) The IR laser is widely tunable (2.35 - 3.40 μm), enabling a large variety of OH rovibrational transitions to be sampled. ii) The IR laser has low frequency noise ($\Delta v \sim 2$ MHz), two orders of magnitude narrower than the typical Doppler widths observed in the cell. The IR laser can therefore be tuned precisely to a given Doppler shifted component (e.g. line center) of a given IR transition. iii) The IR frequency is continuously tunable in segments as long as 0.8 cm^{-1}; these can be overlapped to form arbitrarily long scans. For perspective, the Doppler widths of typical OH transitions are only $\sim$ .01 cm^{-1}. Even in the pressure broadening studies, in which these line widths are the subject of investigation and are deliberately increased, the FWHM is still never more than $\sim$2-3 x 10^{-2} cm^{-1}. The Doppler line shapes can be accurately determined by scanning the IR laser frequency, for

determinations of integrated absorption strengths or to determine collision-al broadening contributions. iv) The fast detector rise times (<1 μs) allow OH reaction and energy transfer kinetics to be observed in real time as a function of OH quantum state. v) The high sensitivity of the IR absorption detection (quantified below) allows high S/N with low concentrations of OH and HNO_3 or H_2O_2 precursor. These low precursor concentrations in turn suppress unwanted chemical reactions in the flow cell. vi) The radicals are formed and probed in a column at the center of the cell, several centime-ters away from the walls. Therefore, OH reaction chemistry can be studied with no contributions due to the heterogeneous wall reactions.

The CH_4 + rare gas energy transfer studies require quite a different experimental arrangement. Here, at least, the molecule under study is chemically stable and can be bought and used directly from the lecture bottle. However, in the crossed jet experiments the target gas and the col-lider gas are introduced through *pulsed* supersonic pinhole nozzles. The CH_4 is therefore a transient species in the vacuum chamber, and the time gated IR absorption technique again serves as an excellent probe of initial and final scattering states. Therefore, even though the experimental envi-ronment is clearly different, the detection principles are essentially the same as those employed for the OH transients.

Briefly, the CH_4 target molecule is seeded in Ar and cooled into its lowest rotational state via supersonic expansion through the prima-ry pulsed pinhole valve. Rotational excitation occurs via collisions with a pulse of collider gas from the secondary pulsed jet. The populations of CH_4 in the jet intersection region are monitored via weak fractional attenuation

of the color center laser light. The column integrated populations in each initial and final scattering state for a given Doppler velocity subgroup is determined from the IR absorbances via Beer's law. The growth of these IR absorption signals as a function of crossing gas concentration provides a measure of the rates of collisional energy transfer into each j state, and hence of the *integral*, state-to-state cross sections for rotational energy transfer. For a given j, the IR absorption signal as a function of Doppler shift provides a measure of the velocity of CH_4 in the laboratory frame (and by simple transformation, in the center of mass frame) and therefore can be used to determine the *differential* scattering cross sections.

Naturally, the IR absorption technique has a number of advantages in the crossed jet experiments. i) The wide tunability not only of the color center laser, but also of available difference frequency, diode, and Ti:Sapphire lasers [Agrawal 1986, Canarelli 1991, Pine 1974] covers the entire near IR spectral region. Since most molecules absorb in the IR, the infrared laser absorption technique is an extremely general and versatile one. ii) The inherently narrow Doppler profiles observed in the jets (~ 0.01 cm^{-1}) offer as much as 10^4-fold higher resolution than techniques such as time of flight mass spectrometry [Scoles 1988]. The fine structure splitting of CH_4 arising from the nuclear spin states of CH_4, for example, are only $\sim 0.01 - 0.1$ cm^{-1} and yet for almost all transitions appear as fully resolved lines in the IR spectrum. iii) The Doppler profiles of initial and final scattering states are directly obtained by scanning the IR laser frequency. This allows straightforward determination of absorption strengths summed over all Doppler shifts for determinations of *integral* energy transfer cross sections.

Furthermore, as mentioned above, since the Doppler profiles reflect the speed and direction of CH_4 as a function of scattering state, it is possible to infer center of mass *differential* scattering distributions from the observed Doppler line shapes.

In this chapter, the experimental arrangements are described. The IR laser operation and characteristics are presented in detail, including descriptions of ancillary optical equipment to measure the IR frequency and verify single mode lasing. Operation and maintenance of the excimer laser follow. Next, the construction and operation of the flash kinetic spectrometer is described, with discussion of the gas handling system and flow cell, laser alignment, IR detection method, and detection sensitivity. In the following section, the preparation and purification of HNO_3 and H_2O_2 photolysis precursors is discussed. Next is a description of the Fourier transform infrared spectrometer and the method by which OH is formed and detected. Finally, the crossed jet spectrometer is described.

Color Center Laser

A great deal of effort has been put toward developing narrow bandwidth ($\sim 2 - 10$ MHz), cw lasers which provide tunable light throughout the near IR. Currently there is a broad array of choices including lead salt diode lasers, Ti:sapphire lasers, color center lasers, and several difference frequency schemes which collectively cover the spectral region from 1.2-10 μm. Our IR source is a color center (Burleigh FCL 20) laser. The phrase "color center" refers to crystals into which electrons or ions are deliberately placed as point defects, a process which often results in bright color-

ation. The name "F center" is also used and comes from the German "Farbe" which means "color". By pumping properly doped crystals with light from a suitable laser (e.g. an ion laser), population inversion can be created and some of these crystals can be made to lase. A number of cw and pulsed color center lasers, with output in the near IR, have been reported in the literature and are well reviewed [German 1985].

The lasing media in the Burleigh laser comprise three crystals. One of these ("crystal 1") can be made to lase from ~2.35-2.50 μm, and is pumped with blue/green light from an Ar^+ laser; this crystal adds negligibly (if at all) to the range of lasing frequencies provided by the other two crystals, and in any event is not used for the experiments described herein. A second crystal ("crystal 2", KCl doped with Li) lases continuously over the range ~2.35-2.9 μm. The third crystal ("crystal 3", RbCl doped with Li) provides laser output from ~2.6-3.4 μm. The crystals are maintained at 77 K. Cryogenic temperatures are needed to prevent thermal migration of the dopant ions, which destroys lasing action.

The color center laser (see Fig. 2.1 for a schematic diagram) is pumped with red light from a Kr^+ ion laser (Coherent Innova K3000). Operation of this ion laser is straightforward and well described in the manual, but a few items are worth mentioning. With clean Brewster windows, rear reflector, and output coupler the laser output is $\geq$ 1 W at 40 Amps, and should be 5 W at the highest attainable current (65 Amps). While the lasing threshold is ~ 38 Amps, the current generally should not be allowed to fall below 40 Amps to avoid strain to the power supply passbank. A light flow of N_2 is directed across the Brewster windows to prevent the buildup of
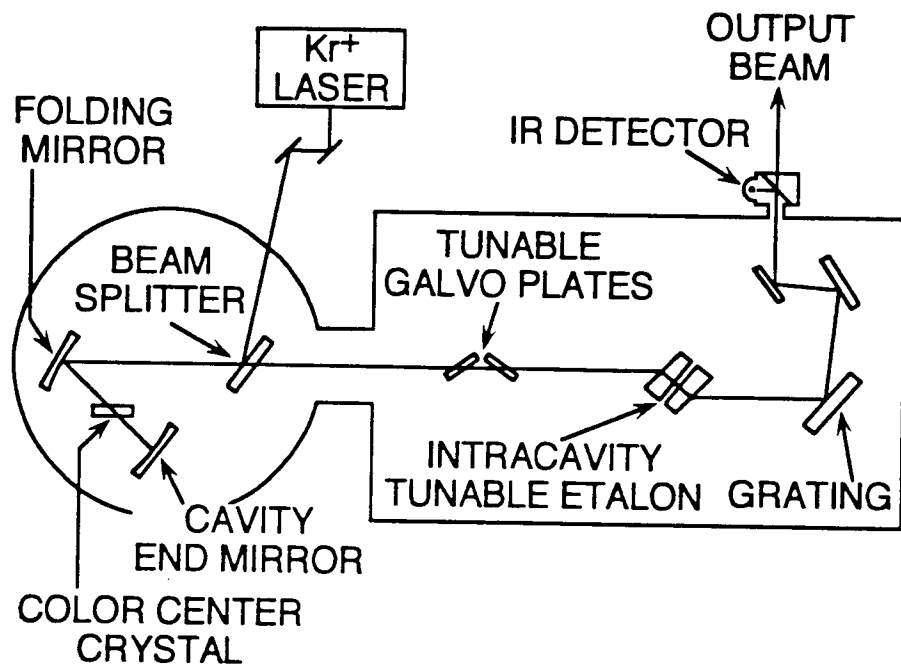
Figure 2.1   Arrangement of the color center laser.

burned-on particulates which can occur in the intense, intracavity laser fields. Periodically, contaminants do settle on the laser optics but generally are easy to remove by cleaning with spectral grade methanol. The amount of power which can be used to pump crystal 3 is limited by the ability of this crystal to dissipate any absorbed energy which is not re-emitted as laser light. Despite the liquid nitrogen cooling, this crystal can overheat and experiences "rollover" at pump powers of 1.1 - 1.3 W [German 1986]. This is recognizable by the rapid decrease followed by cessation of lasing output as the Kr^+ laser power is raised further. Typically, crystal 3 is pumped with 0.7 - 0.8 W, well below the levels at which rollover is observed, and an order of magnitude larger than the threshold (~ 70 mW at 3 μm) for laser action in the FCL. Typical pump power on crystal 2 is 1.3 - 1.5 W, which is sufficient to generate several mW of single frequency IR output. Rollover has not been observed on this crystal even for pump powers >2W.

The versatility of the IR laser spectrometer derives in part from the wide tunability of the F center laser. "Mode hop" scanning of this laser has been used by many groups to generate discrete scans over approximately 1 cm^{-1} by stepping sequentially over 300 MHz (0.01 cm^{-1}) longitudinal modes of the laser cavity [Kryo 1982, Gudman 1983]. This method of tuning is advantageous to accelerate long searches for transitions in systems whose spectra are not well known. However, it is frequently necessary to tune the laser frequency *continuously*. As one example, Chapter 6 describes measurements of line shapes for OH rovibrational transitions which are only a few hundred MHz wide, and which clearly cannot be adequately mapped out in 300 MHz steps! In the commercial laser, true continuous

tuning is possible up to a few GHz by PZT tuning of one of the end mirrors. Kasper *et al.* [Kasper 1981] have developed a method for extending this short range tuning to scans many wavenumbers long. Their method, which has been adopted by several groups [Kryo 1985, Huang 1986, Bryant 1988]], relies on resetting the PZT after each scan segment, advancing the intracavity etalon and the grating which serves as output coupler, and monitoring and overlapping Fabry-Perot fringes from dual cavities over a long sequence of a few GHz scans. This impressive scheme does require an elaborate computer interface, and while the requisite software exists and works reliably it is not always the best solution. For example, we often need to tune the laser a fixed frequency (e.g. to the peak of a transition) and maintain that frequency for many minutes. PZT creep makes such a prospect difficult. Furthermore, the computer is often busy doing other things and it is convenient to be able to tune manually, as well as under computer control, over long frequency ranges.

As an alternative scheme, the color center is modified using well developed strategies for tuning cw dye lasers [Nelson 1988]. The idea is this: the laser cavity length is tuned continuously by intracavity galvo plates, and the intracavity etalon is electronically servo locked to following the scanning laser longitudinal mode. First, the laser frequency is roughly adjusted with a grating, which serves as end mirror and output couples in zeroth order. The laser is operated in a single longitudinal mode in the standard fashion by virtue of the intracavity etalon. The laser power is monitored with a beam splitter mounted inside the tuning arm, which is evacuated (<10 mTorr to prevent arcing at the etalon PZT stacks) to eliminate rather serious absorptions from atmospheric water. A pair of 4mm

thick 90° sapphire plates mounted at Brewster's angle in the cavity can be electronically rotated with galvos; a ~1° rotation of each plate achieves a ~100 μm change in the approximately 50 cm cavity length. By rotating the galvos only ≤2° the laser frequency may be tuned 0.8 cm^{-1}, which is quite sufficient for any of our applications. Introduction of the galvos into the laser cavity results in negligible power loss.

Tuning of the galvo plates alone scans over roughly one free spectral range (FSR) of the laser (0.01 cm^{-1}) before hopping back to the mode of greatest transmission of the etalon. The etalon gain bandwidth is sufficient to allow two adjacent cavity modes to lase simultaneously, so care must be taken that each scan begins with the FCL operating on a single mode (see below). To maintain the same cavity order during the scans and hence tune the laser frequency continuously, the etalon must track the scanning cavity mode and is therefore actively locked to the power maximum of the laser by a servo loop. The galvo driver and etalon servo circuits are both designed in JILA by Dr. John Hall and were originally developed to control the JILA ring dye laser. In order to lock the etalon to the cavity gain maximum the spacing of the etalon plates is dithered at 2 kHz, with an amplitude (≤ 1 V) that is ≤ 10% of that required to hop a cavity mode. This induces a small synchronous modulation of the output power, with a magnitude and phase dependent on the sign of the etalon error. This idea is shown in Fig. 2.2. For a given phase of the etalon dither, the phase of the 2 kHz IR power modulation differs by 180° if the etalon gain curve peaks on the low vs. high frequency side of the lasing frequency. It the etalon is centered at the lasing frequency, the power modulation occurs at twice the
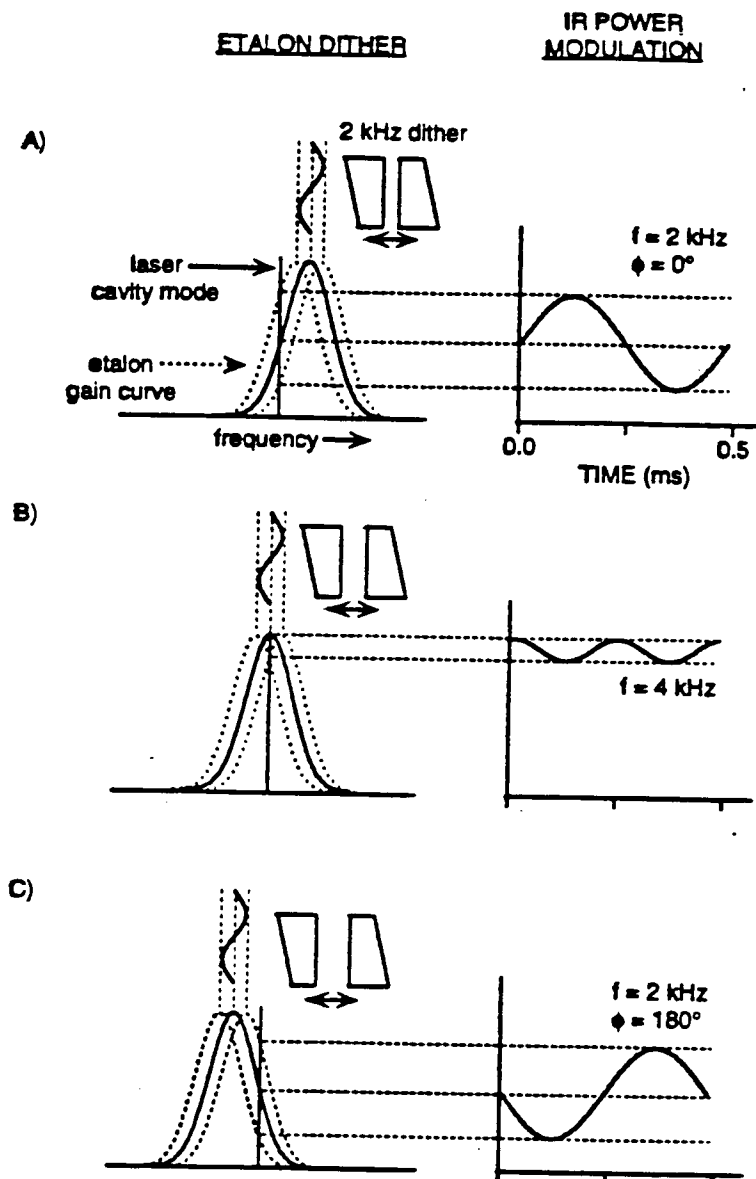
Figure 2.2 Visualization of the etalon servo lock scheme. A small, 2 kHz dither on the etalon results in a synchronous modulation of the output power. The phase depends on the frequency shift between the peak of the etalon gain curve and the laser cavity gain maximum. The error signal is phase sensitively detected and integrated to provide a correction voltage to the etalon plates, thus locking the etalon to the position of maximum transmission at the lasing frequency.

dither frequency, i.e. 4 kHz. A control signal for the etalon is then obtained by phase sensitive detection at 2 kHz of the synchronous power modulation which, after integration, is used to guide the average position of the etalon spacing. The etalon then tracks the galvo tuning of the longitudinal mode. Demands on the loop dynamic range are minimized by feeding forward a linear voltage replica of the galvo drive current to the etalon PZT. Since the bandwidth of the grating is larger than the 0.6 cm^{-1} free spectral range of the etalon, two longitudinal modes separated by this FSR can sometimes both lase. To further ensure single mode operation of the laser for the longest scans, the grating is also tuned with a stepper motor at a rate of 1 step per ~600 MHz. The laser frequency can be scanned by a D/A ramp in frequency increments which are as small as ~ 5 MHz, or by means of a manual potentiometer. Scans over many wavenumbers are accomplished by resetting the laser frequency to the next etalon mode and overlapping sequential scans. With a 0.6 cm^{-1} FSR of the etalon, this provides a comfortable 0.2 cm^{-1} overlap for producing seamless scans of arbitrary length.

In practice, such long scans are not always so painlessly achieved. In fact repeatable scanning without mode hops presents an operational challenge, if not an intellectual one. Proper alignment of the laser cavity is critical. The FCL is a high gain system and will readily lase on two longitudinal modes even with the etalon installed, and also exhibits an annoying tendency to lase on its hole burning mode. Fortunately, there is a reliable systematic method for attaining the requisite cavity alignment. First, every few months (or whenever the cavity alignment is suspect) the etalon should be removed from the cavity and its alignment adjusted until

concentric Newton rings from a transmitted HeNe laser beam are observed as the PZT stack is scanned. The etalon is angled in the cavity so that the retroreflected Kr^+ tracer spot is centered on the left hand edge of the intra-cavity iris. The etalon requires ~ 9 - 10 V to hop between adjacent cavity modes. If the measured voltage is appreciably larger, the angle of the etalon is adjusted in small increments until 9 - 10 V is attained. Next, the cavity folding mirror is moved all the way in (note that the control knob is geared and thus turns all the way *out*), and then is backed off ~ 1.5 turns. This is necessary to suppress the hole burning mode. Single frequency operation is verified by monitoring transmission fringes from a scanning Fabry-Perot etalon, and by looking for the absence of mode beating in the IR interference fringes from a λ meter (see below). The end mirror and grating tilt angle are both adjusted to maximize output power, as measured by chopping the IR beam and monitoring the AC coupled voltage output of a PbS photoconductive detector. A competing laser frequency sometimes appears and is not the next longitudinal or etalon mode. This unwanted frequency (which may be a transverse mode) can be completely extinguished by closing the intracavity iris to a diameter of a few mm.

The filtered and demodulated error signal from the etalon servo provides a particularly useful check of the FCL alignment. The demodulation is performed digitally, with a very high Q multiplexer triggered synchronously with the 2 kHz etalon dither. By tuning the etalon voltage back and forth over the peak of the lasing frequency, both phases of the non-zero error signal should appear with equal amplitude. Any observed asymmetry is an unmistakable signature of misalignment, and the laser will not

scan reliably.

The fun of working with invisible laser beams wears off fast. It is useful to be able to *see* (with the eye rather than an IR detector) the IR laser path much as one can see, say, a dye laser beam. A bit of the red Kr^+ laser beam makes its way out of the FCL cavity, and serves as a decent first order tag locating the IR for very short distances away from the color center laser. However, the Kr^+ and the IR beams follow appreciably divergent paths, making this weak red tracer spot a poor indicator of the IR position downstream on the laser table. In order to establish a completely reliable, visible tracer spot, the IR beam emerging from the FCL is merged with red light from a HeNe. The overlapped IR/red light is then split into several beams. One portion is sent to signal and reference detectors for the flow tube or crossed jet experiments. Another fraction goes to a 10 cm long absorption cell containing reference gas to aid in finding spectral transitions in the crossed jet experiments. Yet another split-off IR beam is sent to a confocal Fabry-Perot etalon (free spectral range (FSR)=151 MHz, finesse~7) whose length is modulated via 30 Hz sawtooth modulation of a PZT. When the IR laser frequency is tuned, the time delay from the beginning of each sawtooth cycle to the appearance of the first interference fringe is measured and saved as a voltage via time-to-amplitude conversion (TAC). The TAC output as a function of laser frequency is thus a sawtooth with peaks separated by the free spectral range of the etalon; any laser mode hops are readily detected as discontinuities in the TAC output.

The frequency noise of the free running color center laser is ~ 2 MHz, which corresponds to a ~2×10^{-8} of the lasing frequency. In order

to tune the IR output precisely to known spectral absorption features, it is necessary to monitor the IR frequency with high precision. This is accomplished in a λ meter, a type of traveling Michelson interferometer invented in JILA by Dr. John Hall [Hall 1976]. The two arms of the interferometer are formed with back-to-back corner cube mirrors mounted on a cart which travels on an air bearing. The optical geometry shown in Fig. 2.3. The IR beams emerging from the two arms of the interferometer are combined on a beamsplitter and monitored as a function of time on a fast IR photodiode. The frequency of the resulting interference fringes is proportional to the IR laser frequency ν_{IR}, though it clearly depends on the speed of the cart as well.

In order to determine the IR wavelength without the need to measure the cart speed to absurd precision, a set of reference interference fringes is generated by the output of a single frequency HeNe laser which occupies the same optical path. While the IR and visible fringe frequencies both depend on the cart speed, their *ratio* is independent of this quantity. Since the HeNe laser frequency ν_{vis} is well known, then the IR frequency is determined (neglecting air dispersion) from

$$\nu_{IR} = \frac{\nu_{IR\,fringe}}{\nu_{vis.\,fringe}} \nu_{vis} .$$

(2.1)

In practice this ratio is determined by sending both the IR and HeNe fringes through a discriminator, and counting the number of IR zero crossings which occur during a preset number ($\sim 10^5$) zero crossings of the discriminated visible fringes. One difficulty of this approach is that the zero crossing circuitry can only detect integral numbers of fringes. This imposes a
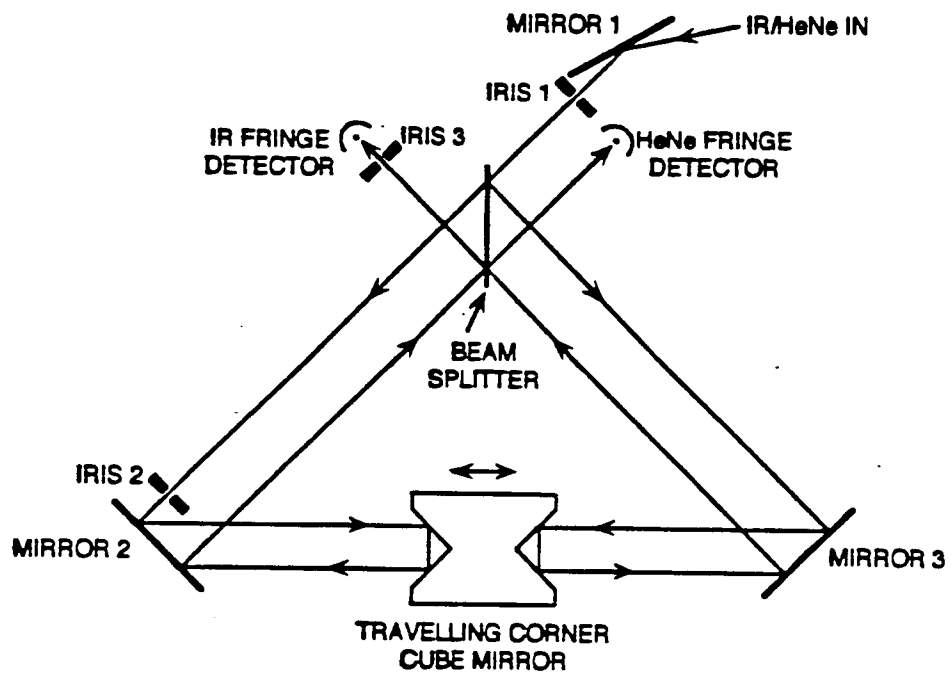
λ METER OPTICAL LAYOUT

Figure 2.3   Optical layout of the λ meter.

limitation on the precision with which the IR frequency can be determined, since the number of IR interference fringe cycles is inherently rounded down to the nearest integer number. To improve this situation, the IR fringes are fed into a phase locked loop which contains a x16 frequency multiplier, thus reducing 16-fold the uncertainty in the last fringe. With this approach, the IR frequency can be measured to a precision of .0005 cm^{-1}.

There is one other practical difficulty with this scheme. The gain bandwidth of the HeNe laser is sufficiently broad for two frequencies to lase simultaneously, separated in frequency by several GHz. If these adjacent modes colors are introduced into the λ meter, mode beating will occur which can destroy the fringe contrast. The two lasing modes can make most efficient use of the gaseous gain medium if they are orthogonally polarized, which tends to happen spontaneously. Therefore, the power in one of the modes may be conveniently eliminated from the beam with a polarizer. Unfortunately, as the length of the laser tube drifts with small changes in the room temperature the power will shift between the two modes and the transmitted polarization will periodically drop out. Such power drifts can be prevented by active stabilization of the laser tube length by heating or cooling the tube to counteract ambient temperature changes. The scheme we use is known as "polarization stabilization" [Balhorn 1972]. The method is shown pictorially in Fig. 2.4. First, the tube is warmed to a few degrees above room temperature with a DC current through 20 Ω heater tape. The two orthogonally polarized HeNe output beams are split in a polarizing beam cube, and the respective power levels are continually sampled on photodiodes. The voltage difference between the two light levels is ampli-
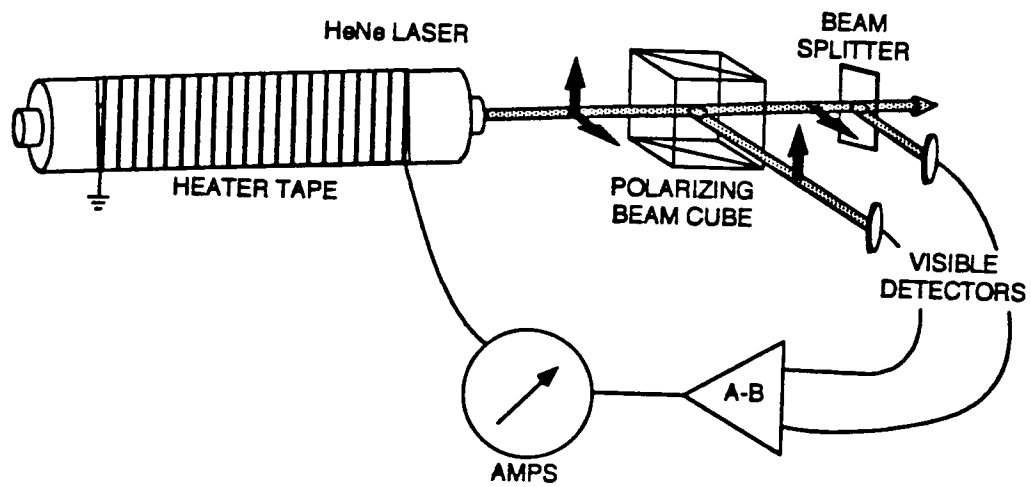
HeNe LASER POLARIZATION STABILIZATION SCHEME

Figure 2.4   Pictorial view of the poarization stabilization arrangement for the HeNe laser.

fied, sent to a discriminator, and the resulting error signal is converted to a current which adds or subtracts as needed from the heater tape supply.

Proper alignment of the IR light into the Fabry-Perot and λ meter is essential. As an arbitrary but convenient standard, the visible and IR beams are defined to be 4.00" above the optical table. To ensure that the laser beams trace a reproducible optical path from day to day, a pair of adjustable irises (4.00" high) are placed along the main beam path, and the laser light is steered precisely through them. Alignment of the red light can be done visually. The IR light is chopped and monitored after the second iris with a PbS photoconductor. During the alignment procedure both irises are partially shut to attenuate the IR by ~ 50%. The infrared beam is then steered with a pair of mirrors until maximum amplitude on the detector is achieved. Additional pairs of irises are similarly used to align the laser beams into the flow cell or crossed jet chamber, and into the Fabry-Perot, λ meter, and reference gas absorption cell when implemented.

The initial alignment of the λ meter merits a few words. With sufficient care it is possible to start from scratch and achieve large amplitude, uniform fringes in under a half hour. The following procedure refers to Fig. 2.3. First, the incoming light is passed through the beam splitter (toward the outside edge), and the transmitted portion is centered through the irises 1 and 2 to establish the usual 4.00" height. With the cart removed, the light is then steered with mirror 2 toward mirror 3; a temporary iris is used to maintain the beam height. The light path is parallel to the track and offset from its center by ~ 1 cm; this offset may need to be smaller if the retroreflected beam misses the beam splitter. Next, the angles of the beam splitter and mirror 3 are tuned until the reflection from mirror 3 overlaps that from

mirror 2. The cart is then placed on the track. If the beams which enter and emerge from the corner cube mirror are at a different heights, then the height of the cart is adjusted with shims as needed. The retroreflected beams should both return one spot on the inside edge of the beam splitter. The final alignment is accomplished by establishing perfect overlap of the light from both arms of the interferometer, and by ensuring that the retrore-flected beams are not steered by the motion of the cart. To do this, mirror 3 is blocked with a note card and the light which returns from mirror 2 is observed on iris 3. Initially this spot probably moves both horizontally and vertically as the cart travels down the track. This motion is eliminated with compensating adjustments from mirrors 1 and 2. When the HeNe tracer spot exhibits no more motion and is centered on iris 3, then the note card is moved to block mirror 2. The other beam is similarly adjusted with the beamsplitter and mirror 3. When both beams are centered on iris 3 and are stationary as a function of cart position, strong fringes should be observable on both detectors. If these fringes do not exhibit constant amplitude as the cart moves across the length of the track, the last stages of alignment should be redone. Typical IR and red interference fringes are shown in Fig. 2.5.

Excimer laser

In the flash kinetic experiments, the OH radicals are formed by pulsed laser photolysis of HNO_3 or H_2O_2. The photolysis source is an excimer laser (Questek 2040) run on the 193 nm (ArF) or 248 nm (KrF) laser lines. The physics of excimer lasers is well reviewed in the literature [Rhodes 1979]. Essentially, a rare gas atom is ionized in a pulsed discharge
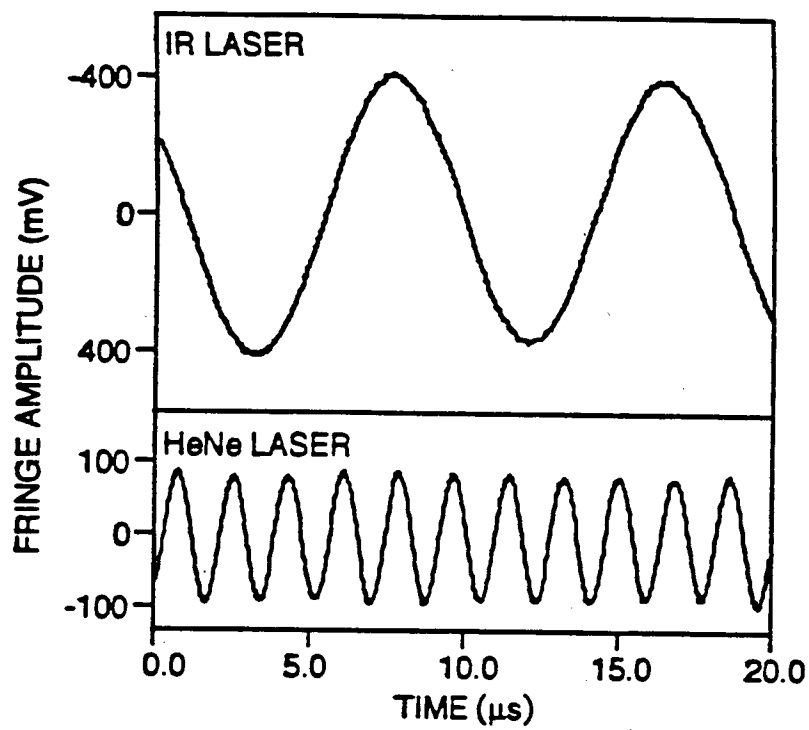
λ METER INTERFERENCE FRINGES

Figure 2.5   Typical infrared and visible λ meter fringes.

and subsequently reacts with a halogen-containing species (F_2 for the laser colors used herein) to form an excimer. Since an excimer by definition is bound in its electronically excited state but dissociative in its ground state, population inversion is automatically created. The laser cavity optics consist of a rear reflector and output coupler in an unstable resonator geometry, which minimizes beam divergence (0.3 mrad). Since the output coupler is uncoated MgF_2, the UV light makes only a few passes through the discharge region before exiting the chamber. Run in this configuration, an excimer laser is really more of a super-radiant light source than a true laser, but since coherence of the output beam is not required in our experiments this poses no difficulties. The bandwidth of the light is several hundred wavenumbers [Rhodes 1979]. Since HNO_3 and H_2O_2 exhibit unstructured absorption features over ~10^4 cm^{-1} [DeMore 1987], the excimer laser line width is sufficiently narrow to photodissociate these precursors with a well defined photolysis cross section. At a 10 Hz repetition rate, the output fluences are $\geq$ 120 mJ/pulse at 193 nm and 400 mJ at 248 nm. Pulse to pulse reproducibility is better than 5%.

The laser is straightforward to operate and requires little maintenance. NiF_2 dust, which forms from reactions of F atoms with the discharge electrodes, can form and tends to settle on the MgF_2 laser optics. A measurable drop in output power is a clear indicator. With regular use, these optics require cleaning every few weeks. Generally a light drag of spectral grade methanol with a lint free lens tissue is sufficient. Care is taken during these cleanings not to exert pressure and thereby scratch the soft substrates. Occasionally the dust will burn onto the optics and form a visi-

ble layer in the shape of the UV beam. This is removed with a dilute SnO_2/ CH_3OH polishing paste, which is rubbed very lightly over the surface with a lens tissue. The SnO_2 is removed by multiple methanol rinses and is followed by one or more light methanol drags. This procedure should be performed as infrequently as possible, to avoid damage to the surface of the MgF_2 optics.

The gas lifetimes of both ArF and KrF are both rather limited. A typical ArF fill will last an hour or two at 10 Hz before the power output drops measurably. The useful lifetime of a given fill is extended to ~ 1 full day through use of a closed cycle recirculator, which removes impurities by trapping them out in a copper coil cooled to 77 K. KrF gas lifetimes are 1 - 2 days; the liquid nitrogen recirculator cannot be used, since Kr liquefies at 121 K [Weast 1989]. In principle the KrF lifetimes could be extended with a warmer recirculator (e.g. with dry ice or an H_2O/CH_3OH slush bath), though this has not been necessary nor implemented in our laboratory.

IR flash kinetic spectrometer

The flash kinetic spectrometer (Fig. 2.6) requires the continuous introduction of gases into the flow cell. These gases include the HNO_3 or H_2O_2 photolysis precursor, buffer gas, and an alkane in the case of the OH reaction rate measurements. It has proven extremely useful to construct a pyrex gas handling system to store and purify the various gases, and to allow in situ preparation of the HNO_3 via the chemical reaction/ vacuum distillation procedure which will be described shortly. The gas handling rack, shown schematically in Fig. 2.7, consists of 1" diameter pyrex seg-
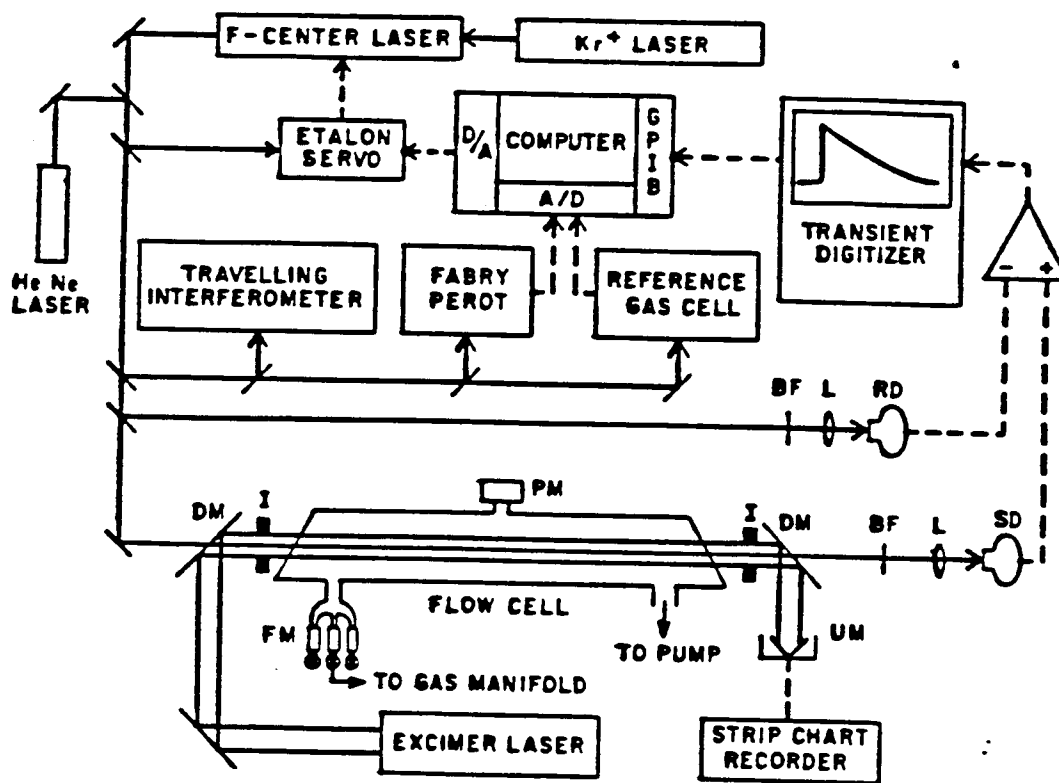
Figure 2.6   Schematic of the infrared flash kinetic spectrometer. DM = dichroic mirror; FM = mass flowmeter; PM = pressure meter (capacitance manometer); I = adjustable iris; BF = bandpass filter; UM = ultraviolet power meter; L = lens; SD = signal InSb detector; RD = reference InSb detector.
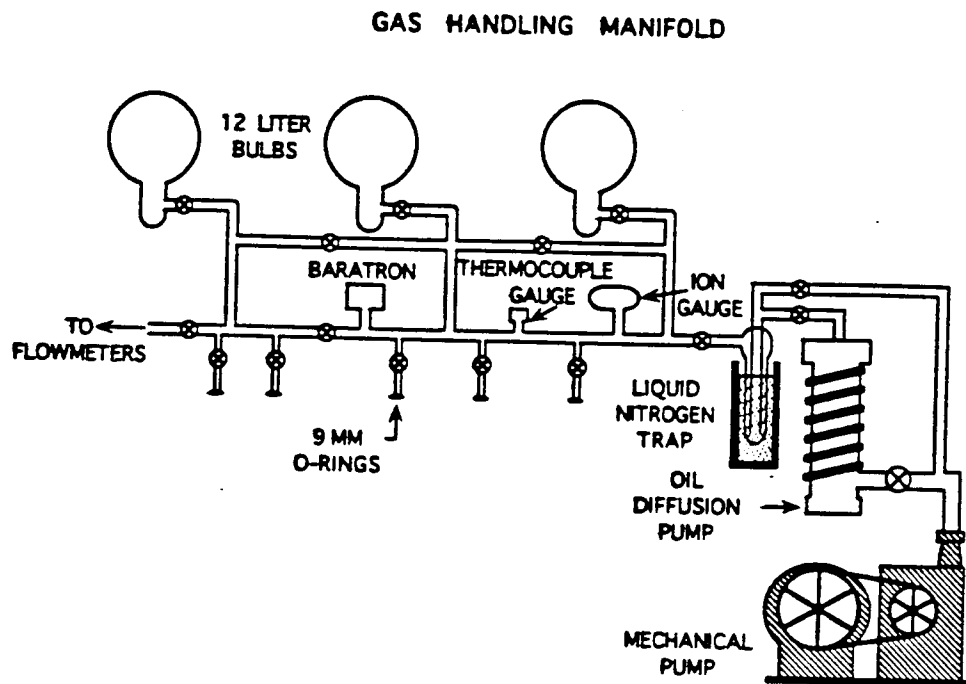
Figure 2.7 Schematic of the pyrex gas handling system.

ments separated by stopcocks. Gases can be introduced through a number of 9 mm O ring joints separated by stopcocks from the main rack. Three 12 liter bulbs are also included in the system and are used for storing premixed gas samples. The entire system is pumped by a 2" diffusion pump backed by a ~5 cfm mechanical pump; an inline liquid nitrogen trap is included to prevent backstreaming of pump oil into the gas handling system, and to reduce the ultimate pressure to ~ 1×10^{-6} Torr.

The center of the flash kinetic spectrometer is a pyrex flow tube (5.0 cm diameter, 97 cm length), equipped with IR quartz end windows angled to deflect the reflected UV from the illuminated column. The HNO_3 or H_2O_2 precursor and any buffer or reagent gases are introduced from the gas rack into the cell at the upstream end. The gases are pumped with a linear velocity of ~ 30 cm/s by a cryo-trapped 40 cfm mechanical pump (Welch 1375). The total cell pressure is monitored with a 100 Torr capacitance manometer (Baratron 222CA) at the center of the cell. Inline stopcocks are included at the entrance and exit of the cell so that the flow may be stopped and experiments performed with static fills. In order to prevent reactive species (e.g. HNO_3) from reaching the pump and to eliminate backstreaming of the mechanical pump oil into flow cell, a three stage cryo-trap is installed upstream of the mechanical pump. At the end of each day this trap is sealed off at both ends with stopcocks, the liquid nitrogen is removed, and the trap is purged with a light flow of air through a second pair of stopcocks. The air flow out of the trap is sent through a polyflow tube to a chemical hood, and into a container of water so that positive air flow can be verified from the resulting steady stream of bubbles.

The absolute concentration of each constituent gas is an essential quantity in the studies of OH reaction rates, and frequently proves useful for a number of systematic checks in the other experiments. For example, the purity of the HNO_3 can be tested by in situ measurements of the UV absorption cross section, as measured by the UV laser attenuation as a function of HNO_3 concentration. In order to determine the partial pressures, the gases enter the cell through a mass flowmeter (Tylan FM280)/ stainless steel needle valve combination. The sole exception is H_2O_2, which is introduced into the flow cell only through a needle valve to preclude the possibility of decomposition which could conceivably occur by contact with a heated flowmeter element. The flowmeters are calibrated by timing the rates of a series of pressure rises into a calibrated volume (generally the flow cell); the partial pressure of each gas in a given experiment is calculated from the flow rates and the total cell pressure. Note that since only the *relative* flow rates (but *absolute* pressure) are needed, the flowmeters may be calibrated in any relative units. However, in order to estimate the mean lifetimes of gases in the cell it is useful to know the true flow rates in absolute units (conventionally sccm) and thus calibrate the flow cell volume. This is readily accomplished via the ideal gas law by determining the volume of a reference gas bulb from the mass of water it can contain, filling this vessel to a known pressure of gas, and expanding this gas into the flow cell. A typical flow meter calibration is shown in C_2H_6 in Fig. 2.8. A mass flow meter measures the flow rate from the heat transferred to the moving gas and is expected to exhibit highly linear response at pressures which are well out of the molecular flow regime (≥ 1 Torr). The high degree of linearity
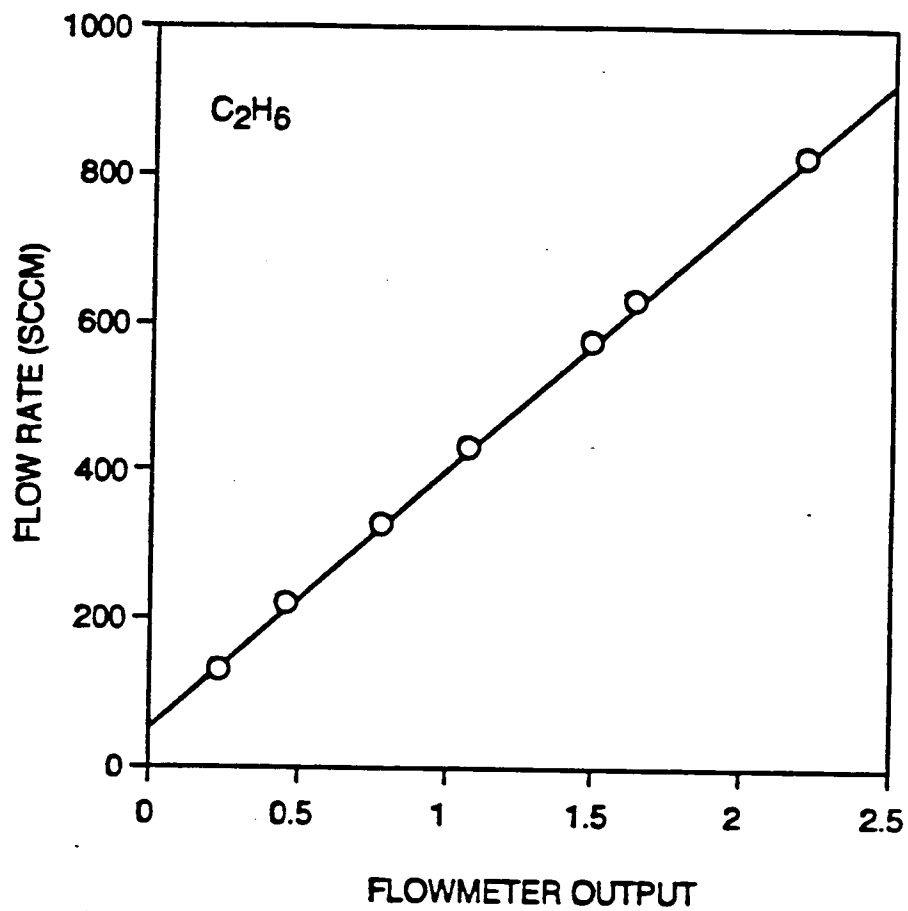
TYPICAL FLOWMETER CALIBRATION

Figure 2.8   Typical flowmeter calibration.

seen in the calibration of Fig. 2.8 is routinely observed, as anticipated.

A key feature in the flash kinetic measurements is a collinear photolysis laser/IR probe laser geometry. By careful overlap of the excimer and color center laser beams, the IR light samples OH radicals formed along the full (97 cm) path length of the flow cell. Since the OH infrared transition moments are measured in part of the work presented in this thesis, and since the absorption path length is known, absolute OH concentrations can be calculated from the fractional attenuation of the IR laser light via Beer's law. For the quantum yield experiments in particular, for which absolute number densities of the absorbed UV photons must be determined accurately, it is also important to ensure that the excimer laser pulses exhibit a uniform spatial profile. In order to ensure maximum uniformity, the central circular portion of the 1 x 3 cm beam is selected with a variable iris located in front of the cell entrance window, transmitting only 3 mJ at 193 nm and ≤ 12 mJ at 248 nm. The 10 ns pulses, limited to a 9.6 Hz repetition rate to minimize precursor depletion and to avoid buildup of chemical reaction products, are coupled into the cell with an 85% UV reflecting, 95% IR transmitting dichroic mirror. On exiting the cell, the transmitted UV is directed onto a disk calorimeter with a second dichroic mirror. The power incident on the calorimeter, which is calibrated by comparison with a second power meter and a pulse energy meter, is monitored on a strip chart recorder. The IR probe beam is telescoped to a <4 mm beam diameter (95% power) at the cell input so that it comes to a soft focus inside of the cell, and is rendered collinear with the UV beam through the dichroic mirror. Both the IR and UV beams are aligned through irises on either end of the cell, and thus the IR light only samples radicals formed at the center of the larger diameter

photolysis beam. The transmitted IR, as well as a reference IR beam, are focused with CaF_2 lenses (f=2.5 cm) onto 0.25 mm diameter, 77 K InSb photovoltaic detectors. IR bandpass filters (2.5 - 3.5 μm half-power points) eliminate the weak, much broader band pulsed IR output from the excimer laser discharge. Copper shielding around the detectors reduces radio-frequency pickup from the excimer laser to negligible levels.

The IR light level is maintained at $\leq$ 25 μW, well within the linear operating range of the photovoltaic detectors. We have explicitly measured the response of the InSb detectors as a function of IR power by monitoring the apparent absorption of a rotating glass slide (a very convenient nonsaturable absorber) as a function of IR power. The absolute power is measured for each run with a thermopile (Eppley). The results of this test are displayed in Fig. 2.9; the detector response is seen to be extremely linear. At higher IR powers this plot exhibits downward curvature indicative of detector saturation. At $\leq$ 25 μW the IR power is also orders of magnitude less than would be required to saturate an OH transition at the $\leq$ 100 Torr cell pressures used in any of the experiments.

The outputs from the signal and reference detectors are balanced in a fast differential amplifier to subtract the common mode laser amplitude noise. For this purpose we have used a Tektronix 7704A analog oscilloscope which is readily configured to subtract and amplify two voltages. The signals are summed in a 125 MHz digital storage oscilloscope (Lecroy 9400) to improve the signal to noise ratio (S/ N), and stored in an IBM compatible, 80286 based micro computer. The sensitivity of the detection system is 10^{-6} / $\sqrt{Hz}$, or 5×10^{-4} in the 250 kHz detector bandwidth.
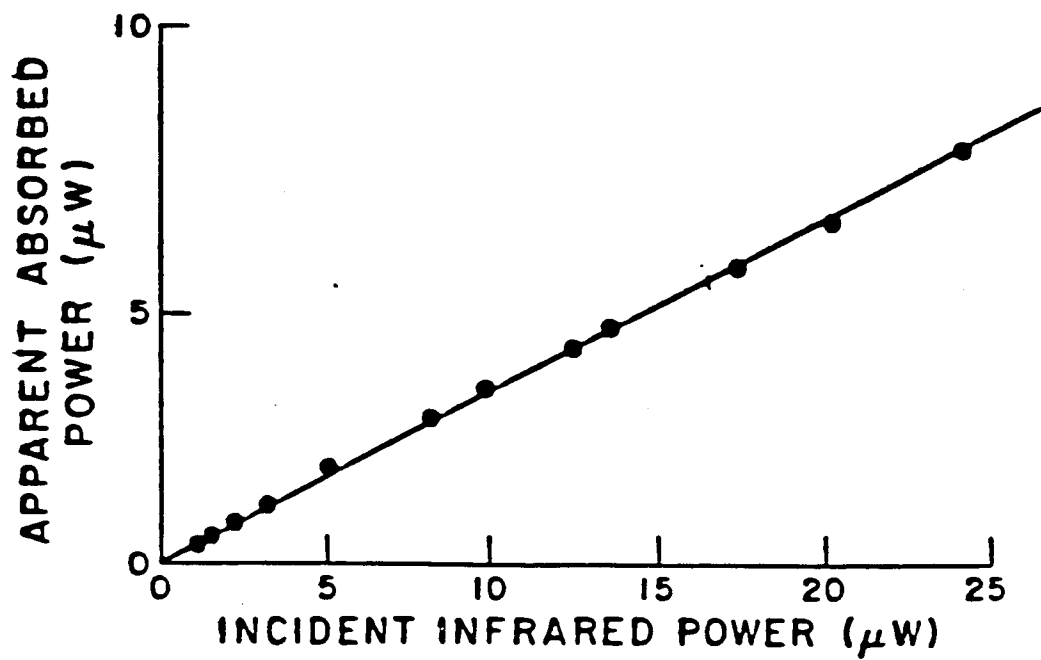
Figure 2.9 Demonstration of the linear response of the signal InSb photo-
voltaic detector with respect to incident laser power.

The rise time of the system is measured to be <1 μs, measured as the response (10% - 90% amplitude points) of the signal InSb to a pulse from an IR LED. It is also possible to measure the rise time in a way which more directly mimics a typical experiment, by inserting an acousto-optic modulator (AOM) in the IR beam path and deflecting a small fraction of the IR light with square edged pulses to the AOM. In order for this to work, the IR should be lensed to a tight focus so that the transit time of the acoustic wave across the IR beam contributes negligibly to the observed response. It turns out that a typical commercial AOM that is antireflection coated for a HeNe laser (we have a few, culled from old FAX machines) can Bragg diffract as much as 10% of the IR, a much larger fraction than is typically absorbed by OH. Casual, late night efforts have shown that this approach does work as anticipated.

A typical IR absorption trace is shown in Fig. 2.10. Such time resolved signals from the LeCroy are saved as binary files with the BASIC program TIMETRAC. The signal is measured on the OH P(3.5)1$^+$ (v=1←0) transition with 7 mTorr of HNO_3 and 9 Torr Ar buffer gas. The rise time is ~ 1 - 2 μs and reflects the time scale for rotational relaxation of the nascent OH(N≤20) [Schifman 1993]. The decay time is considerably longer, lasting several ms and is primarily due to diffusion of the OH out of the probe region. Note that between the fast rise and the slow decay, there are three orders of magnitude to play with. OH *reaction* rates can thus be measured over a wide range of decay times, allowing accurate determination of reaction rate constants. The peak fractional attenuation, indicated by the back extrapolation over the linear portion of the decay shown in the figure, is
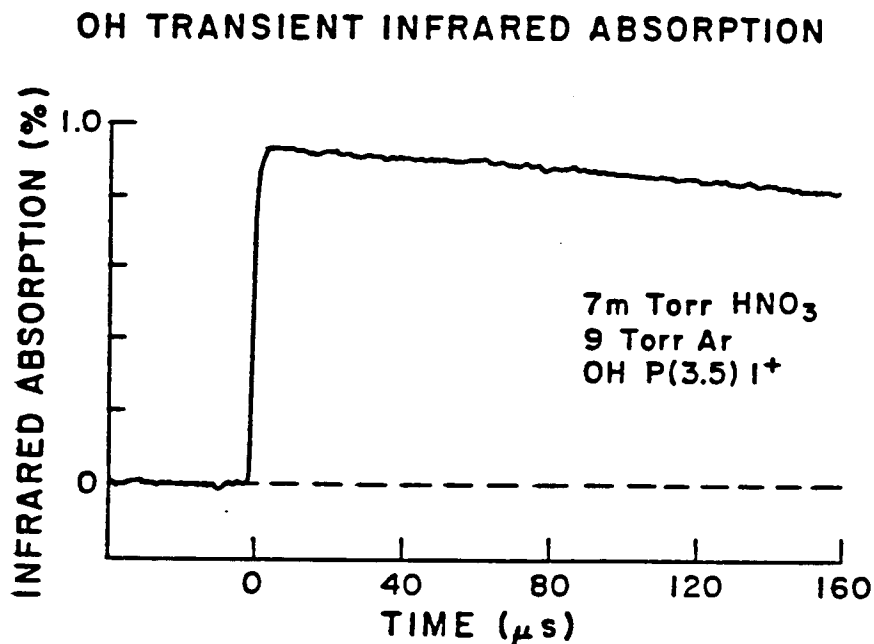
OH TRANSIENT INFRARED ABSORPTION

Figure 2.10 Typical infrared absorption time trace for OH in the flow cell, measured on the P(3.5)1$^+$ transition (v=1←0). This signal is the average of 100 time traces, recorded with 9 Torr of Ar and 7 mTorr of HNO$_3$ flowing in the cell.

<1% and the linear limit for Beer's law applies. The IR absorption signals are thus directly proportional to the concentrations of OH in each quantum state.

In order to map out the spectral line profiles for transitions of OH in the flow cell, the time dependent absorption signal at a given frequency is averaged for ≤ 32 pulses, with 20% of the resulting time trace taken prior to the excimer laser pulse to establish the zero absorption level. To provide a measure of the frequency dependent absorption, the time integral of the resulting decay is integrated in the computer. It is clear that there is an optimal upper limit on the time integral, since integration to a small fraction of a decay time cannot take advantage of the benefits of noise averaging while integration out to many decay times is sampling mostly noise. Assuming for simplicity a single exponential decay and random (white) noise, it is straight forward to calculate the number of decay lifetimes which should be integrated for maximum S/N. Denoting N_{rms} as the noise level on the observed time trace, integration will reduce this noise by

$$N_{int} \propto N_{rms}/\sqrt{T} ,$$ (2.2)

where T is the is the upper limit of the time integral, and N_{int} is the effective noise level after this integration. If the signal S(t) decays as

$$S \propto e^{-at} ,$$ (2.3)

then the integrated signal S_{int} will scale as

$$S_{int} \propto \left(1 - e^{-aT}\right) .$$ (2.4)

The signal to noise ratio is then

$$\frac{S_{int}}{N_{int}} = \frac{\left(1 - e^{-aT}\right)}{N_{rms}\sqrt{T}} \ . \tag{2.5}$$

The optimum value of T is determined by taking the derivative of Eq. 2.5 with respect to T, setting the result equal to zero, and solving the resulting transcendental equation for T. From this analysis, the optimum value of T turns out to be ~ 1.25 1/e decay times.

The OH line shapes are then mapped out by scanning the IR laser over each transition in 10 MHz steps under computer control. The scanning is performed under control of the BASIC program SCANBOX. Signal averaging turns out to be faster in the computer rather than in the LeCroy, and so is performed with the assembly routine AVER. The integration is performed with another assembly routine called ADDLOOP. Interference fringes from the Fabry-Perot etalon are acquired simultaneously with each OH line shape to provide frequency markers of known (151 MHz) spacing .

Preparation and purification of HNO_3 and H_2O_2

In principle, the OH radical could be made a number of ways. For example, in one common technique $O(^1D)$ atoms are photolytically generated from a precursor such as N_2O, and OH is produced by the fast reaction of $O(^1D)$+ H_2O [Tully 1986]. Of course, such chemical reactions can introduce a number of potential chemical contaminants into the system, may take tens of μs to go to completion, and can populate several vibration-

al levels which are slow to relax [Rensberger 1989]. In contrast, OH can be directly generated via UV photolysis, an effectively instantaneous method of production with respect to the 1 - 2 μs rotational relaxation time observed under typical cell conditions. The question thus arises: which precursor? HNO_3 is a particularly attractive answer for two reasons. First, it can be made with very high purity using simple vacuum distillation techniques. Secondly, the absorption cross section at 193 nm is unusually large ($\sigma_{193}^{HNO_3} = 1.3 \times 10^{-17}$ cm^2) [DeMore 1987], enabling efficient photolytic generation of OH with small precursor concentrations. Specifically, with a typical UV fluence in the flow cell of 3 mJ and 10 mTorr of HNO_3, ~30% of the UV photons will be absorbed resulting in [OH]~4.3×10^{13} cm^{-3}. Such concentrations can be observed via IR absorption with S/N of ~50-100 for the most highly populated states.

Pure HNO_3 is prepared [Stern 1960] either from (i) the dehydration of 70% HNO_3 by excess H_2SO_4, or (ii) as the product of the reaction between 70% H_2SO_4 and $NaNO_3$. The former method is definitely preferred, since the $NaNO_3$ powder tends to become an indisposable, solid, cement-like lump with the latter technique. In either case, the HNO_3 is doubly distilled under vacuum and stored as a solid at 77 K to prevent thermal decomposition. The acid is then warmed to 0° C, sometimes even to room temperature, for use as the OH precursor. The high purity of the acid is established via measurements of the absorption cross sections at 193 nm and 248 nm, which are found to agree closely with the reported values [DeMore 1987]. For the measurements of OH radiative lifetimes and quantum yields, the nitric acid is introduced into the flowmeter directly from the va-

por pressure [Stern 1960]. However, in order to measure appreciable changes in OH line widths for the pressure broadening studies, it is necessary to work at buffer gas pressures in the cell as high as ~ 100 Torr, an inherent nuisance given the 30 Torr vapor pressure of HNO_3 at room temperature. Consequently, in order to provide sufficient backing pressure for positive flow into the cell at all total pressures used for these studies, a 300 Torr mixture is made by dilution of 30 Torr of HNO_3 in the collision gas (M) to be investigated. This HNO_3/M mix is stored in the 12 liter bulbs, which in turn have been pre-passivated with several aliquots of HNO_3 gas, to provide a sufficient reserve for a full day of experiments.

H_2O_2 is also employed as an OH precursor, largely due to its importance in the chemistry of the earth's atmosphere [Brasseur 1986, Spivakovsky 1990]. From a pragmatic experimental standpoint, however, it is far less convenient than nitric acid. First, the absorption cross sections are considerably smaller at both excimer laser wavelengths, with $\sigma_{193}^{H_2O_2} = 6.1$ x 10^{-19} cm^2 and $\sigma_{248}^{H_2O_2} = 9.0$ x 10^{-20} cm^2 [DeMore 1987]. Second, it cannot be run through a mass flowmeter without risk of decomposition. Third, its vapor is necessarily mixed with H_2O which could conceivably introduce unwanted chemical reaction channels in the flow cell. Nonetheless, with sufficient care these difficulties can be surmounted as described in detail in Chapter 5. The liquid H_2O_2 is concentrated from a commercial 70:30 H_2O_2:H_2O mixture by driving off excess H_2O for several weeks in a bubbler with a stream of He. The resulting H_2O_2 is ~ 85% pure, as estimated from the vapor pressure at 0° C [Stern 1960]. Since the cell pressure is gen-

erally ~ 9 Torr in the quantum yield experiments, and the vapor pressure of the H_2O_2 is only ~ 4 Torr, the H_2O_2 is introduced into the cell with a stream of He.

Fourier transform infrared spectrometer

During the course of our measurements of OH transition moments, we found it advisable to look directly at emission from OH in highly vibrationally and rotationally excited states. Such studies, which provide intensity information about OH (v>0), nicely complement the IR laser absorption studies which explicitly probe populations in OH (v=0). For completeness, we have also used the FTIR spectrometer in absorption mode, to record v=1←0 spectra. Fourier transform emission spectroscopy (FTIR) is a well established technique for high resolution (≤0.05 cm^{-1}) spectroscopic studies of IR emitters. Fortunately for us, Dr. Carleton Howard at NOAA has an excellent FTIR setup which has been optimized to produce and detect free radicals with remarkable efficiency. All of our FTIR studies have been performed in his laboratory, with the assistance of Dr. John Orlando and Dr. James Burkholder.

An overview of the Fourier transform spectrometer (FTS) is given in Fig. 2.11. Detailed descriptions of its operation and performance characteristics are presented elsewhere [Burkholder 1987]. The infrared chemiluminescence from excited OH radicals is detected by a liquid nitrogen cooled InSb photovoltaic detector followed by a low noise transimpedance amplifier. The spectra obtained span the region from 1975 to 7200 cm^{-1} with a CaF_2 beamsplitter used throughout. The window of the emis-
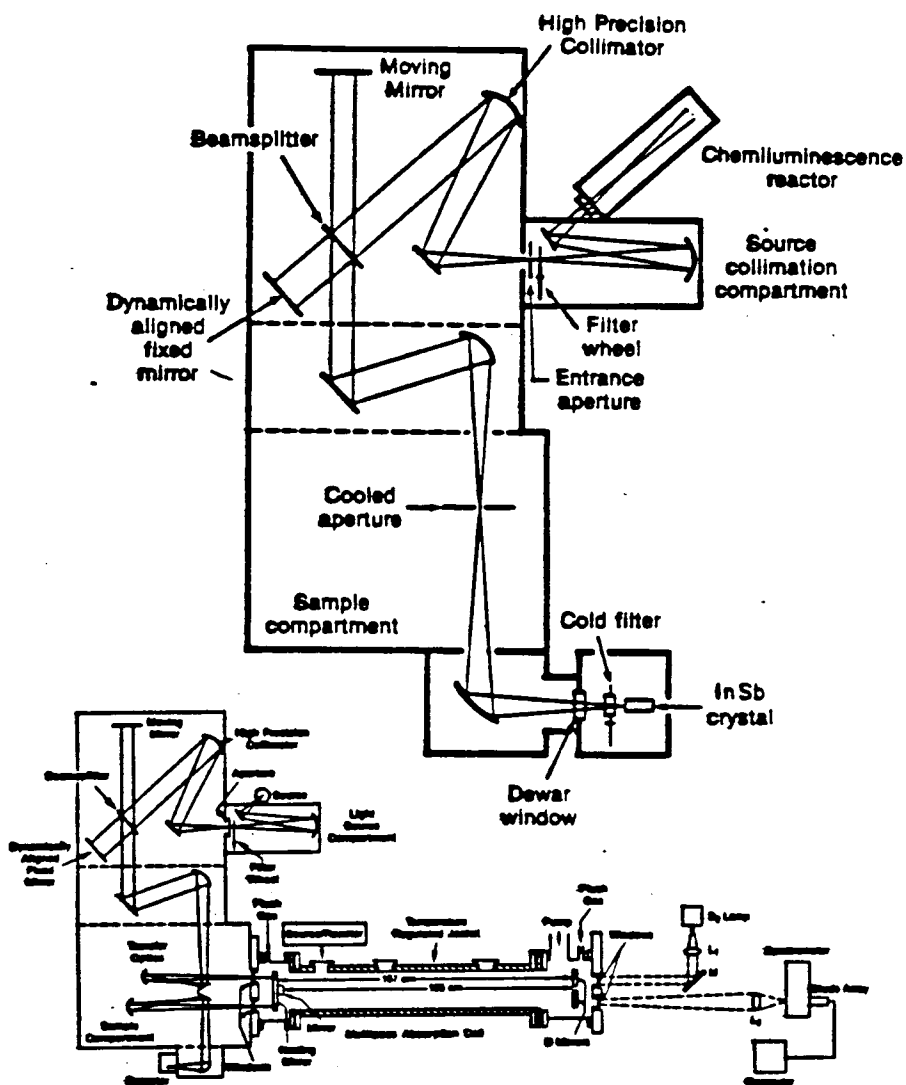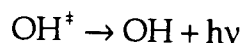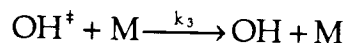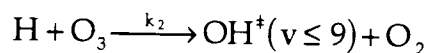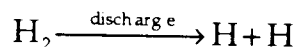
FOURIER TRANSFORM SPECTROMETER

Figure 2.11 Schematic of the Fourier transform infrared spectrometer. The top and bottom traces, respectively, are the configurations for measurements of OH ($v \leq 9$) emission and OH ($v=1 \leftarrow 0$) emission.

sion cell is KBr. For most scans the spectral resolution is 0.05 cm^{-1}. The highest S/N ($\sim$ 200:1 on strong lines) is obtained in the $\Delta v=-1$ scans with $v'\leq 7$ where a liquid nitrogen cooled 4.5 µm short pass filter is employed. This filter reduces broad band noise on the detector by limiting background blackbody radiation from the FTS. Alternatively, scans without this filter are acquired with a dry ice cooled aperture placed at the first image of the entrance aperture to reduce background radiation. For each scan, the aperture size is selected according to spectral range and resolution requirements. For all emission spectra the aperture diameter is 3.5 mm. The phase characterization of the interferograms is carried out using a quartz halogen lamp placed inside the emission cell. The interior of the spectrometer is purged with He or dry N_2 to eliminate infrared absorbing species in the beam path.

The OH is formed in the emission cell by the reaction of H atoms with ozone. The essential chemistry is given by

$$H_2 \xrightarrow{\text{discharge}} H+H$$

$$H+O_3 \xrightarrow{k_2} OH^{\ddagger}(v \leq 9)+O_2$$

$$OH^{\ddagger} + M \xrightarrow{k_3} OH + M$$

$$OH^{\ddagger} \rightarrow OH + h\nu$$

where OH‡ denotes vibrational excitation. The enthalpy of the H + O$_3$ reaction ($\Delta H=-322$ kJ/mol) [Baulch 1982] is sufficient to populate the OH(v=9) level from room temperature reactants. Since we are interested in OH rovibrational radiation, it is clearly essential to minimize the rates for vibrational relaxation of OH during the $\sim$ 10 ms mean residence time in the emission

cell. H atoms are the most efficient relaxers present with k_3 (v=1,2)=3 x 10$^-$^{10} cm^{3}molecule^{-1}s^{-1} [Spencer 1976]. It is therefore reasonable that the best results should be obtained with an excess of O_3 (with respect to H) flowing into the emission cell. Indeed, excess ozone does produce optimal signal strength and the signals continue to grow with increased O_3 flow up to the highest flow rates utilized. The OH formation time in the cell is estimated to be ~ 200 µs (k_2=2.8 x 10^{11} cm^{3}molecules^{-1}s^{-1}) [Baulch 1982]. If the vibrational relaxation of OH by H atoms proceeds at a near gas kinetic rate for all v, the relaxation process would also occur on a ~ 200 µs time scale, thus explaining the sensitivity to O_3 concentration.

Optimized experimental conditions for recording the OH emission data are as follows. The total pressure in the emission cell is 0.6 Torr, 99% of which is He carrier gas. The total input flow rate is 20 sccm. The initial O_3 concentration is ~ 2 x 10^{14} cm^{-3} whereas the initial H atom concentration is estimated at ~ 2 x 10^{13} cm^{-3} based on 50% dissociation of H_2 in the microwave discharge. The residence time of the gases in the spectrometer field of view is ~ 10 ms. Fig. 2.12 shows a typical emission spectrum.

In addition to recording the OH vibrational emission, the FTS was also used for remeasuring v=1←0 absorption intensity ratios from a more nearly room temperature OH (v=0) source. This provides an additional redundancy check on the intensity ratios determined with the flash kinetic laser spectrometer. The OH radicals for the absorption experiment are formed by the reaction of F atoms with H_2O:
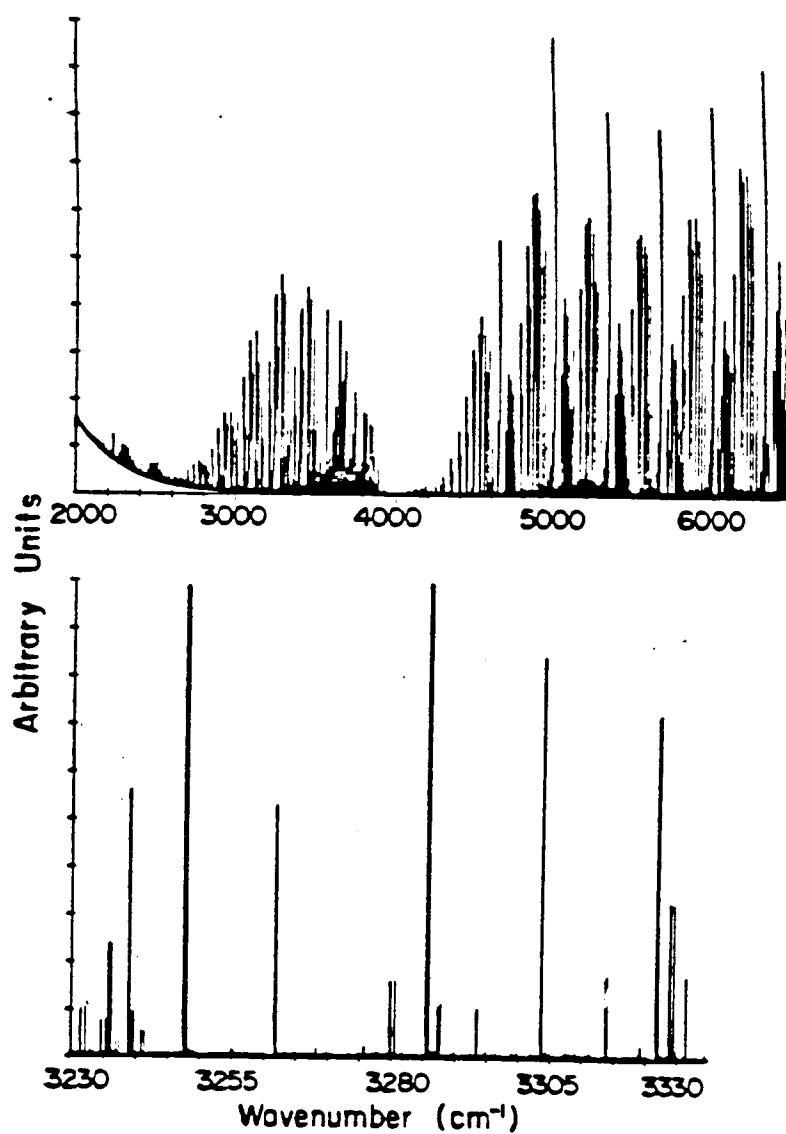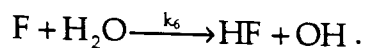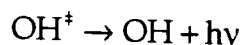
Figure 2.12 (a) Low resolution plot of the OH infrared emission observed for the H + O$_3$ source. (b) Expanded plot of the spectrum in (a) illustrating the resolved rotational structure and signal to noise in the OH emission.

$$OH^{\ddagger} \rightarrow OH + h\nu$$

$$F + H_2O \xrightarrow{k_6} HF + OH .$$

Although this reaction is sufficiently exothermic to populate OH (v=1) [Baulch 1982], the observed spectra are consistent with a near room temperature OH rovibrational distribution. The total pressure in the absorption cell is 0.75 Torr and the total flow rate is 130 sccm, resulting in a much larger OH residence time in the cell of ~ 100 ms. The H_2O is carried into the cell by flowing He gas through a H_2O bubbler. The initial H_2O concentration is estimated at ~ 2 x 10^{14} cm^{-3} based on the partial pressure and flow rate of H_2O in the He/H_2O mixture. The initial concentration of F atoms is estimated at ~ 1 x 10^{13} cm^{-3}, based on a 30% dissociation efficiency for F_2. Under these conditions the OH formation time is estimated to be ~ 300 μs (k_6=1.1 x 10^{-11} cm^{3}molecule^{-1}s^{-1}) [Baulch 1982] and an OH vibrational relaxation time faster than ~ 400 μs (k_3=1.4 x 10^{-11} cm^{3}molecule^{-1}s^{-1}) [Smith 1985] considering only the relaxation by H_2O. These time scales are clearly much shorter than the OH residence time in the absorption cell and thus the OH rovibrational distribution is fully relaxed to a v=0, nearly room temperature rotational distribution.

Fig. 2.12 shows the configuration of the spectrometer during the absorption measurement. The light source is a quartz halogen lamp. As in the emission work, a CaF_2 beam splitter is employed and the light is detected with a liquid nitrogen cooled InSb photodiode. A room temperature 2.5 μm long pass filter is used to eliminate high frequency IR source radiation. Inclusion of a White cell [White 1942] provides an absorption path

length of 99.2 m. The limiting aperture diameter is 1.5 mm. The spectrometer body is evacuated to minimize spurious absorptions in the same spectral region by the strong asymmetric stretch mode of H_2O. The spectrum covers the $v = 1 \leftarrow 0$ absorption band, spanning the region from 3520 - 3900 cm^{-1}, with a resolution of 0.01 cm^{-1}.

In both the emission and absorption measurements the He (99.9 % pure) buffer gas is passed through a trap containing molecular sieve material at 77 K for further purification. For the emission experiments, O_3 is prepared by passing O_2 through an ac discharge and collecting the ozone on silica gel maintained at dry ice temperature. The O_3 is ~ 90% pure with O_2 as the major impurity. The hydrogen gas (> 99.9 % pure) is diluted in He to 4% concentration and used without further purification. For the absorption experiments a commercial mix of 5% F_2 in He is used directly from the cylinder.

Crossed jet apparatus

From the thermal conditions of the flow cell, and the complex world of chemistry in the FTS, we now plunge into the rarefied environment of crossed atomic and molecular jets. The crossed jet apparatus represents the newest addition to our laboratory, and has just graduated from incipient, first generation status to a reliable experimental tool for measurements of rotational energy transfer cross sections. This maturation has been achieved largely through simple but exhaustive systematic checks on collision probabilities, molecular fluxes, clustering thresholds, linearity of IR signal with increasing target and collider gas concentrations, etc. The re-

sults of such tests have dictated the choices of operating conditions and it is therefore worthwhile to describe all details of the experimental arrangement. A general description of the apparatus follows, with aspects specific to CH_4 scattering reserved for Chapter VII.

The crossed jet apparatus is shown in Fig 2.13. The pulsed valves are housed in a vacuum chamber constructed from 3 cm thick aluminum. In order provide sufficient room for infrared multipass optics inside the chamber, and to allow the distance from each valve to the jet intersection region to be varied over a wide range (≤ 12 cm), the chamber volume is 40 cm per side for an internal volume of ~67 liters. A square hole is cut from each of the side and top faces, leaving a frame with a 5 cm border onto which clear plexiglass flanges (40 cm per side, 3 cm thick) are mounted on O-ring seals. The transparent sides provide visual access to the inside of the chamber, thereby facilitating the alignment of the valves and infrared laser light under vacuum. All pulsed valve feedthroughs, CaF_2 windows to pass the IR laser beam, and vacuum gauges are on smaller aluminum flanges mounted to the large plexiglass sides. The chamber is pumped through a liquid nitrogen cooled baffle with an oil diffusion pump (CVC PVMS-1000A, 4000 liters/s) backed by a Roots blower (Edwards EH1200/E1M275, 500 liters/s). Chamber pressure is monitored by a thermocouple gauge and an ion gauge, and is $\leq 5 \times 10^{-6}$ Torr (1 Torr = 133 Pa) without the valves. Due to small residual leaks around the valve, the chamber pressure rises to $\leq 5 \times 10^{-5}$ Torr with both valves installed but not operating. However, this corresponds to a mean free path one or more orders of magnitude larger than the size of the chamber, ensuring that residual background gas does not contribute to ro-
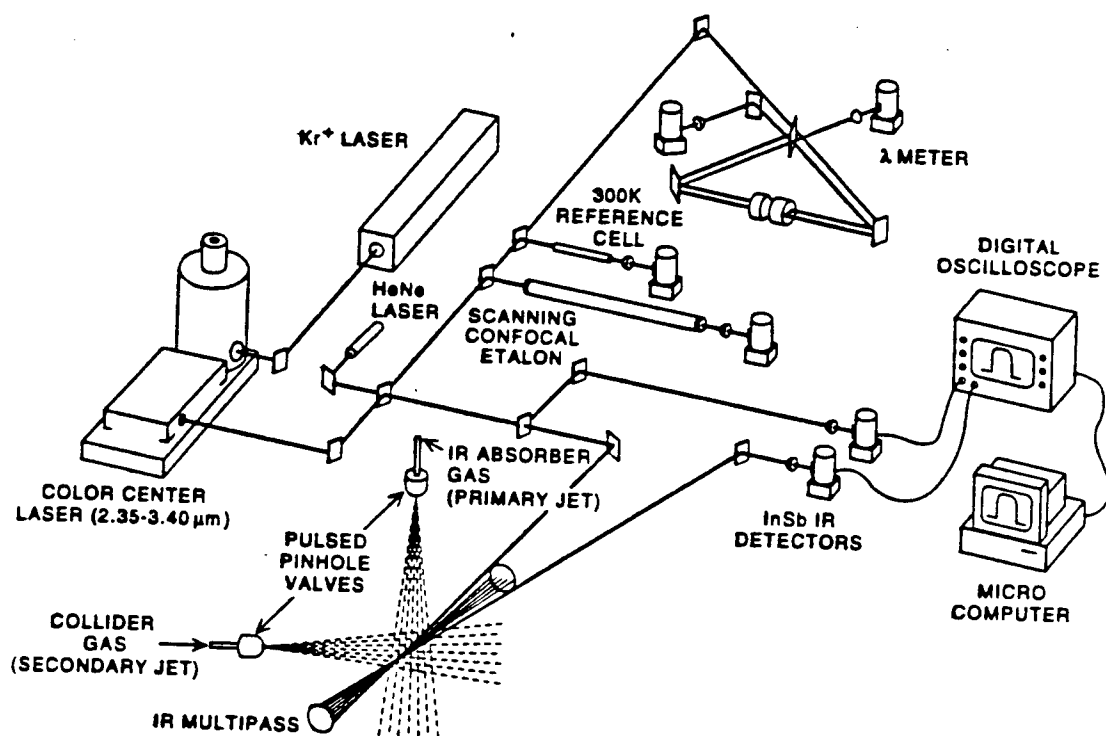
Figure 2.13 Schematic of the crossed jet/infrared laser apparatus.

tational excitation of the target gas.

The target (also denoted "primary") and collider ("secondary") jets are formed through pulsed pinhole nozzles which enter the chamber through O-ring feedthroughs. For the CH_4 + rare gas experiments, the primary valve is a Newport BV100; the collider gas is expanded through a General Valve (GV series 9). Unfortunately, the bulk of the residual leaks into the vacuum chamber are around the Newport valve. Furthermore, this valve is rather large and heavy, and therefore unwieldy and hard to adjust its distance from the jet intersection region. Therefore, the apparatus has recently been reconfigured to accept two General Valves; the chamber pressure now routinely falls below 10^{-5} Torr with both valves off. Both the GV and Newport valves are driven by a current pulse through a solenoid which impulsively withdraws a sealing poppet. The General Valves are actuated with pulse drivers designed in our laboratory. In any case, operation with two *pulsed* valves serves to maintain a low average pressure ($<1 \times 10^{-4}$ Torr) and also allows the relative timing of the jets to be varied. At present, the valves are mounted so that the jet center lines intersect at 90°. In order to tune the collision energy, a mounting system has recently been added which allows the relative intersection angle between the two jets to be varied from 30° - 145°. The distance between each nozzle and the jet region is set to 4.0 cm. The gas pulse durations of the primary nozzle (diameter = 518 µm) and the secondary nozzle (diameter = 159 µm) are adjusted to ~ 500 µs and ~ 1ms respectively, allowing the target gas pulse to sample the uniform temporal center of the longer, collider gas pulse. The valves are pulsed at a rate of ≤10 Hz, limited by the acquisition rate of the data collection system.

The infrared laser beam emerging from the color center laser is first overlapped with red HeNe laser light to establish a visible tracer spot, and then is split into several beams for the λ meter, Fabry-Perot etalon, and CH_4 reference absorption cell. The remainder of the infrared light is split equally into signal and reference beams. The signal portion is directed into the vacuum chamber through a CaF_2 optical flat which serves as both the entrance and exit window. The infrared laser passes through the jet intersection region at 90° to the plane formed by the expansion axes of the two orthogonal jets. It is also possible to propagate the IR beam in the plane of the crossed jets, a configuration which has been shown to be convenient for determinations of angular scattering distributions from Doppler profiles [Serri 1981, Taatjes 1990]. In order to increase the absorption path length, the IR light is first focused into the chamber with a CaF_2 lens (f=50 cm), and then is multipassed $\leq$ 22 times through the jet intersection region with a 30 cm optical cell after the design by Herriot [Herriot 1964]. On exiting the chamber the IR beam is collimated with a second CaF_2 lens (f=50 cm) and is focused onto a 0.5 mm diameter, 77 K InSb photovoltaic detector with a third CaF_2 lens (f=2.5 cm). The reference portion of the infrared beam is similarly focused onto a matched InSb detector. The IR power on both InSb detectors is maintained at $\leq$ 100 μW, where the detector response is found to be linear. The voltage outputs of the signal and reference detectors are limited to bandwidths of 5 kHz with electronic lowpass filters for improved S/N, and (as in the OH experiments) are subtracted in the Tektronix oscilloscope to suppress common mode amplitude noise by a factor of ~ 25. The resulting absorption signal is sent to the LeCroy digital oscilloscope for signal

averaging, and transferred to the laboratory computer via the GPIB cable for storage and analysis. The infrared detection sensitivity in the crossed jet apparatus is 2×10^{-5} / $\sqrt{Hz}$, or 1.4×10^{-3} in the 5 kHz detection bandwidth. For a typical absorption strength of 10^{-1} cm and Doppler widths of ~ 0.01 cm^{-1}, the resulting single pulse detection limit is ~4×10^{10} cm^{-3}. The detection sensitivity is demonstrated in Fig. 2.14, which for reference shows a scan over the $Q(1)F_1$ transition of CH_4, with a peak absorption of 16%. Also shown are the baseline noise levels with the signal detector blocked to demonstrate the S/N improvement due to dual beam subtraction, and with both detectors blocked to show the ultimate noise level of the InSb detectors in the 5 kHz detection bandwidth.

A typical, time resolved IR absorption signal is shown in the top trace of Fig. 2.15. This signal and others shown throughout this paper are taken from our studies of CH_4 - rare gas scattering. It is worth noting for reference that due to the nuclear spin statistics of the H atoms, CH_4 has three ground rotational states (j=0,1,2) labeled by symmetry in the T_d rotational group. These states, which are analogous to the ortho- and para-modifications of H_2, are not interconverted via collisions on the time scale of the expansion pulse. In any event, the top trace in Fig. 2.15 is measured for the primary jet with 210 Torr stagnation pressure of 10% CH_4 seeded in Ar, standard conditions for all data shown herein. The typical IR absorption strength on the ground state molecules is $\leq$ 10%; the corresponding absorption signals for CH_4 in excited states following collisional excitation is $\leq$ 1%. Also shown in Fig. 2.15 is the IR absorption signal observed when the

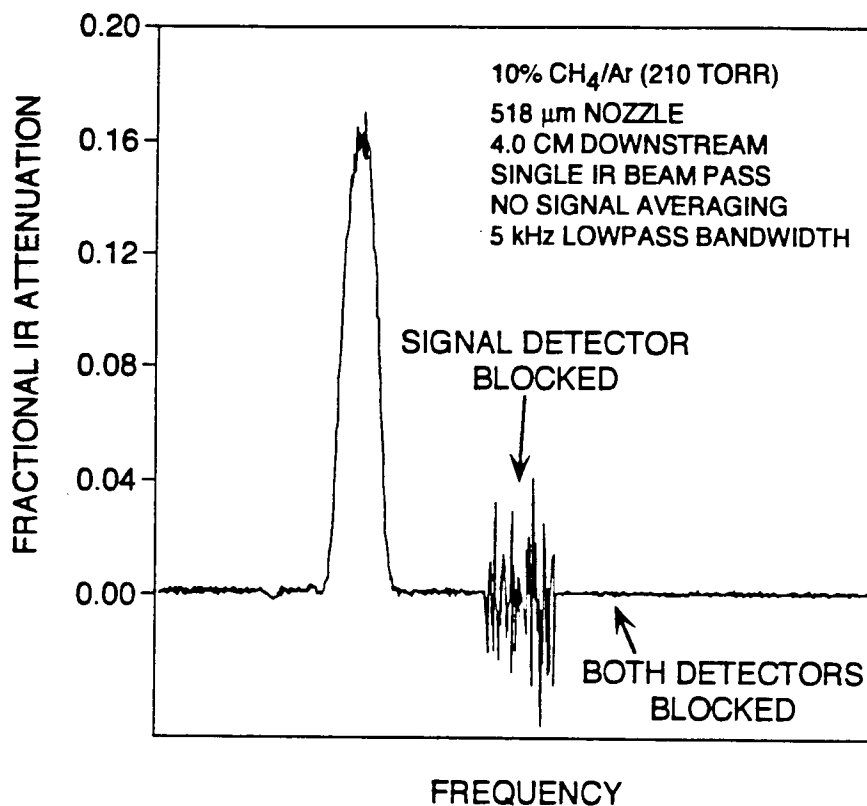## DEMONSTRATION OF INFRARED
ABSORPTION SENSITIVITY

Figure 2.14 Demonstration of the infrared detection sensitivity in the crossed jet experiments. Shown is a scan over the $Q(1)F_1$ (i.e., ground state) CH_4 transition to provide a calibrated absorption scale and thus demonstrate the S/N. The peak absorption is 16%. Also shown is the baseline with the signal detector blocked, demonstrating the large (~25-fold) reduction in common mode noise that is attained via dual beam subtraction, and with both detectors blocked to demonstrate the ultimate noise levels of the InSb detector/amplifier combination.
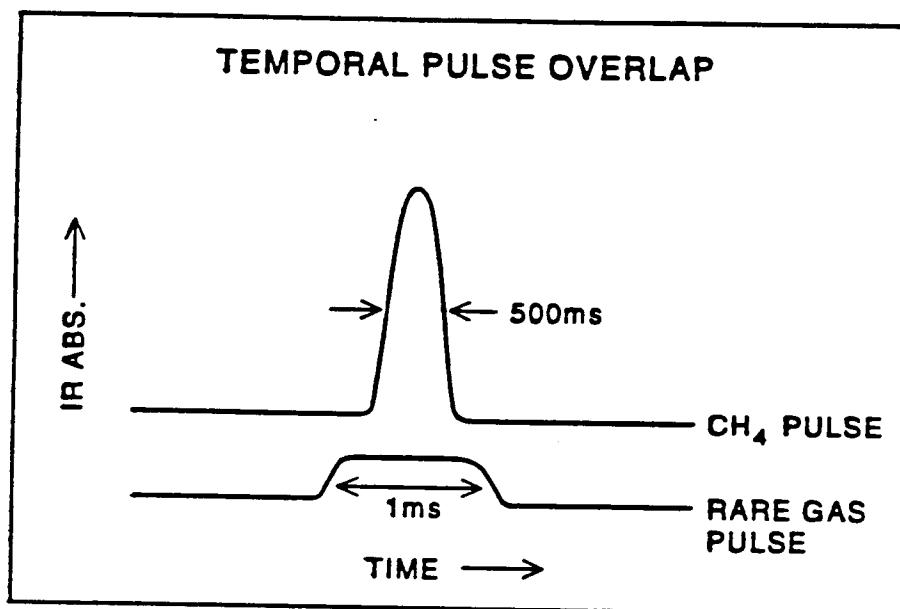
Figure 2.15 Time domain infrared absorption in jet cooled CH_4 (10% CH_4/ Ar mix) for the primary and secondary jets. The ~500 μs primary jet pulse (top trace) is delayed to sample the uniform temporal center of the ~1 ms secondary jet pulse.

CH_4/Ar mix is run through the secondary nozzle, showing the uniformity of the collider gas pulse for the full ~ 1 ms open time of the valve.

In order to measure Doppler profiles of the CH_4 rovibrational transitions, the IR laser is scanned under computer control in 5 MHz steps, using the BASIC program SCANXB. The transient absorption signal at each frequency is averaged for ≤ 32 pulses with assembly language routine AD-DLOOP to increase the S/N. The IR absorption signal is then integrated over the time gate of the gas pulse. In order to determine the zero absorption level, the two adjacent gates before and after the gas pulses are integrated, averaged together, and subtracted from the signal gate. During frequency scans the infrared light transmission through the 300 K cell is also monitored to provide reference spectral peaks. Interference fringes from the Fabry-Perot etalon are acquired using the TAC to provide markers of 151 MHz frequency spacing, providing the frequency ruler necessary to extract center of mass angular scattering distributions from the IR intensities as a function of Doppler shift.

A scan over the R branch [($v_3=1 \leftarrow 0$), 3028-3057 cm^{-1}] of CH_4 in the primary jet is shown in Fig. 2.16. In each spectral scan, the infrared absorption intensity is scaled to the known Honl-London factors. The CH_4 is efficiently cooled with > 96% of the population in each of the three rotational ground state levels. It can be shown [Herzberg 1945] that the ratios of populations in the ground j=0,1,and 2 states are predicted to be 4.9:8.7:2 (see Chapter 8); this ratio is observed, as expected, for the infrared absorption intensities in Fig. 2.16. Based on the small (< 4%) populations observed in excited j states (see Fig. 2.16), the CH_4 is quite cold with a rotational
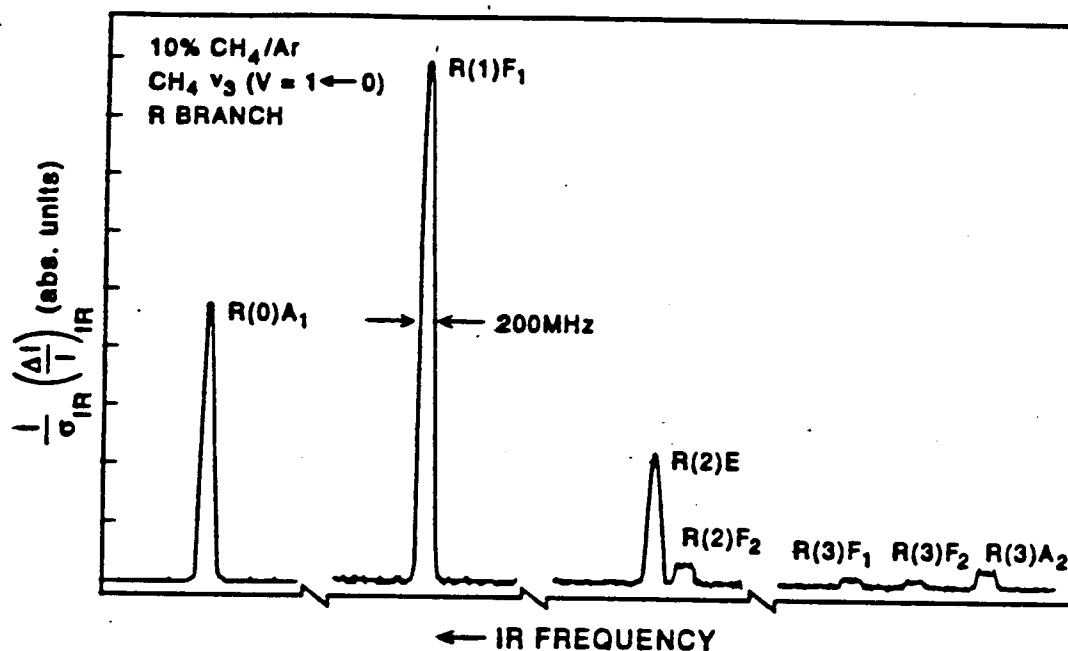
NASCENT POPULATIONS: JET COOLED CH$_4$

Figure 2.16 Scan over the CH$_4$ (ν_3 v=1←0) R branch, demonstrating the efficient cooling of CH$_4$ in the nascent, primary free jet expansion. The rotational temperature is estimated to be ~7-8 K. More than 95% of the population in each CH$_4$ symmetray modification is cooled into its ground rotational state.

temperature estimated to be ~ 7-8 K .

Through the use of low concentrations of collider gas in the jet inter-section region ($<4 \times 10^{12}$ cm^{-3}) the inelastic scattering probability is typical-ly $\leq 10\%$ and therefore dominated by single collision events (see below). For CH$_4$ + rare gases the final scattering states j$_f$ are populated in a single colli-sion from the initial state j$_i$:

$$CH_4(j_i) + \text{rare gas} \xrightarrow{\sigma_{i \to f}} CH_4(j_f) + \text{rare gas} .$$
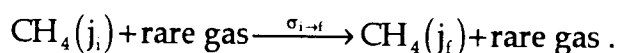
Over this range of collider gas concentrations, the fraction of CH$_4$ excited into a given j$_f$ scales linearly with collider gas concentration:

$$\frac{[CH_4(j_f)]}{[CH_4(j_i)]_0} \approx \sqrt{1 + \left(\frac{v_{\text{rare gas}}}{v_{CH_4}}\right)^2} \; \sigma_{i \to f} \int [\text{rare gas}] d\ell \qquad (2.6)$$

where [CH$_4$(j$_i$)]$_0$ is the initial concentration of CH$_4$ in the ground rotational state. The column integrated rare gas density $\int [\text{rare gas}] d\ell$ can be mea-sured directly, by seeding the rare gas jet with CH$_4$ and measuring the ab-solute, integrated absorption on a convenient ground state transition. The factor $\sqrt{1 + \left(v_{\text{rare gas}}/v_{CH_4}\right)^2}$ is a kinematic correction, necessary because the secondary jet is not stationary but instead has a nonzero laboratory velocity, and arises as follows. The collision rate k is related to the cross sec-tion via

$$k = \sigma_{i \to f}[\text{rare gas}]v_{\text{rel}}$$

$$= \sigma_{i \to f}[\text{rare gas}]\sqrt{\left(v_{CH_4}\right)^2 + \left(v_{\text{rare gas}}\right)^2}. \tag{2.7}$$

For a given interaction pathlength $d\ell$, the CH_4 interacts for a time τ given by

$$\tau = d\ell/v_{CH_4}. \tag{2.8}$$

The collision probability P is then

$$P = k\tau = \sigma_{i \to f}[\text{rare gas}]\sqrt{1 + \left(v_{\text{rare gas}}\right)^2 \Big/ \left(v_{CH_4}\right)^2}\, d\ell \tag{2.9}$$

The cross section $\sigma_{i \to f}$ for each jf is determined from Eq. 2.6 as the slope of

a linear plot of $\dfrac{[CH_4(j_f)]}{[CH_4(j_i)]_0}$ vs. $\sqrt{1 + \left(\dfrac{v_{\text{rare gas}}}{v_{CH_4}}\right)^2}\, \int[\text{rare gas}]d\ell$.

The population $[CH_4(jf)]$ is determined from the infrared absorption signals:

$$\left(\frac{\Delta I}{I}\right)_{IR} = 1 - e^{-\sigma_{IR}[CH_4(j_i)]\ell} \approx \sigma_{IR}[CH_4(j_f)]\ell, \tag{2.10}$$

where $(\Delta I/I)_{IR}$ is the fractional IR attenuation at a given frequency and σ_{IR} is the absorption cross section. The latter half of Eq. 2.10 arises from the magnitude of the typical absorption signals, whch permits the exponential to be expanded out to the linear term. The signals are integrated over all Doppler detunings for each transition to measure the total population in a given jf. The IR laser absorption technique inherently measures number density of the scattered target gas, whereas the cross sections are propor-

tional to the flux. The conversion of concentration to flux is common to many LIF experiments and mass spectroscopic measurements, and has been discussed by a number of authors [Scoles 1988]. The factors by which the j-dependent absorption signals must be scaled depend on the final speed of the target gas, which can be calculated from energy conservation, and on the angular scattering distributions, which must be measured [Mac-Donald 1989]. Since the Doppler profiles provide reflect the differential scattering distributions for each j state (see below), the conversion from number density to flux could in principle be performed by explicit deconvolution of the Doppler line shapes. However, the procedure is involved and in general not necessary. For example, in the CH_4 + rare gas scattering, collisional energy transfer into j≤4 ($\Delta E_{rot}≤105$ cm^{-1}), the final CH_4 velocity changes by ≤20 %. Therefore, the j-dependent velocity will have *at most* a ≤20% influence on the signals observed for these states. As a simple and reasonable approximation, the flux in each j state ($f_j(CH_4)$) is calculated by

$$f_{jf}(CH_4) \approx [CH_4(j_f)] \cdot v_{CH_4}. \tag{2.11}$$

Note that since the infrared laser samples the jet intersection region directly, <u>all</u> scattered target gas molecules will observed. Indeed, we have verified that the sum of populations in all rotationally excited levels is equal to the depletion from the initially populated level in the nascent free jet expansion, indicating that no serious errors are introduced. By measuring the population in each jf as a function of collider gas concentration, the state-to-state, integral cross sections are determined from Eq. 2.6.

For scattering by unstructured collider gas (e.g. rare gases), the rotational excitation occurs solely via the T-R process. Since both jet velocities

are well defined and since the initial and final states of the target gas are known, the final speed of the target molecule in a given j_f is uniquely determined from conservation of energy and lies on a Newton sphere in the center of mass frame. The flux of molecules into a given differential solid angle appears at a characteristic Doppler shift; the observed j-dependent line shapes thus reflect the differential scattering distribution in the laboratory frame, and by simple transformation, in the center of mass frame.

References for Chapter 2

Agrawal, G. P., and Dutta, H. K., *Long Wavelength Semiconductor Lasers* (van Nostrand-Reinhold, New York, 1986).

Balhorn, R., Kunzman, H., and Lebowsky, F., Appl. Opt. **11** 742 (1972).

Baulch, D. L., Cox, R. A., Crutzen, P. J., Hampson, R. F. Jr., Kerr, J. A., Troe, J., and Watson, R. T., J. Phys. Chem. Ref. Data **11** 362 (1982).

Bryant, G. W., Eggers, D. F., and Watts, R. O., private communication (1988).

Burkholder, J. B., Hammer, P. D., and Howard, C. J., J. Phys. Chem. **91** 2136 (1987).

Canarelli, P., Benko, Z., Curl, R. F., and Tittel, F. K., J. Physique IV **1** 1 (1991).

German, K. R., J. Opt. Soc. Am. B **3** 149 (1986).

Gudman, C. S., Begeman, M. H., Pfaff, J., and Saykally, R. J., Phys. Rev. Lett. **50** 727 91983).

Hall, J. L., and Lee, S. A., Appl. Phys. Lett. **29** 367 (1976).

Herriot, D., Kogelnik, H., and Kompfner, R., Appl. Opt. **3** 523 (1964).

Herzberg, G., *Infrared and Raman Spectra,* (van Nostrand-Reinhold, New York, 1945).

Kasper, J. V. V., Pollock, C. R., Curl, R. F. Jr., and Tittel, F. K., Chem. Phys. Lett. **77** 211 (1981).

Kryo, E., Chaghervand, P. S., Eliades, M., Danzeiser, D. A., Lieb, S. G., and Bevan, J. W., Can. J. Chem. **63** 1870 (1985).

Kryo, E., Lieb, S. G., and Bevan, J. W., Rev. Sci. Instr. **53** 1550 (1982).

MacDonald, R. G., and Liu, K., J. Chem. Phys. **91** 821 (1989).

Nelson, D. D. Jr., Schiffman, A., Lykke, K. R., and Nesbitt, D. J., Chem. Phys. Lett. **153** 105 (1988).

Pine, A. S., J. Opt. Soc. Am. **64** 1683 (1974).

Rensberger, K. J., Jeffries, J. B., and Crosley, D. R., J. Chem. Phys. **90** 2174 (1989).

Rhodes, Ch. K., Ed.s, *Excimer Lasers* (Springer-Verlag, New York, 1979).

Schiffman, A., Nelson, D. D. Jr., and Nesbitt, D. J., J. Chem. Phys. **98** 6935 (1993).

Scoles, G. Ed., *Atomic and Molecular Beam Methods* (Oxford University Press, New York, 1988).

Serri, J. A., Kinsey, J. L., and Pritchard, D. E., J. Chem. Phys. **75** 663 (1981).

Smith, I. W. M., and Williams, M. D. J. Chem. Soc. Faraday Trans. 2 **81** 1849 (1985).

Spencer, J. E., and Glass, G. P., Chem. Phys. **35** 15 (1976).

Spivakovsky, C. M., Yevich, R., Logan, J. A., Wofsy, S. C., and McElroy, M. B., J. Geophys. Res. **95** 18491 (1990).

Stern, S. A., Mullhapt, J. T., and Kay, W. B., Chem. Rev. **60** 185 (1960).

Tully, F. P., Goldsmith, J. E. M., Droege, A. T., J. Phys. Chem. **90** 5932 (1986).

Weast, R. C., Ed., *CRC Handbook of Chemistry and Physics, 70th Ed.* (CRC Press, Boca Raton, 1989).

White, J. U., J. Opt. Soc. Am. **32** 285 (1942).